The Planetary Science Journal, 6:174 (16pp), 2025 July https://doi.org/10.3847/PSJ/ade8eb

Orbital Capture of Ejecta into Periodic Orbits around Binary Asteroid (65803) Didymos

Xiaoyu Fu[1], Flavia Saveriano[1], Stefania Soldini[1], Fabio Ferrari[2], Derek C. Richardson[3], Masatoshi Hirabayashi[4], Alessandro Rossi[5], Eugene G. Fahnestock[6], Tony L. Farnham[3], Arnold Gucsik[7], Stavro L. Ivanovski[8], Martin Jutzi[9], Akos Kereszturi[10], Jian-Yang Li[11], Francesco Marzari[12], Colby C. Merrill[13], Fernando Moreno[14], Sabina D. Raducan[9], Juan Luis Rizos[14], Gonzalo Tancredi[15], Josep M. Trigo- Rodriguez[16], Kleomenis Tsiganis[17], Stephan Ulamec[18], Yang Yu[19], Yun Zhang[20], Nancy Chabot[21], Andrew Rivkin[21], Adriano Campo Bagatin[22], and Patrick Michel[23]

[1] Department of Mechanical and Aerospace Engineering, University of Liverpool, Liverpool, L69 3BX, UK; Xiaoyu.Fu@liverpool.ac.uk
[2] Department of Aerospace Science and Technology, Politecnico di Milano, Milan 20159, Italy
[3] Department of Astronomy, University of Maryland, College Park, MD 20742, USA
[4] Daniel Guggenheim School of Aerospace Engineering, Georgia Institute of Technology, Atlanta, GA 30332, USA
[5] Istituto di Fisica Applicata "Nello Carrara" (IFAC-CNR), Sesto Fiorentino 50019, Italy
[6] Jet Propulsion Laboratory, California Institute of Technology, Pasadena, CA 91109, USA
[7] Eszterházy Károly Catholic University, Department of Physics, Eszterházy tér 1, H-3300, Eger, Hungary
[8] INAF Osservatorio Astronomico di Trieste, Trieste, Italy
[9] Space Research and Planetary Sciences, Physics Institute, University of Bern, Bern 3012, Switzerland
[10] Konkoly Observatory, CSFK, HUN-REN, Budapest, Hungary
[11] School of Atmospheric Sciences, Sun Yat-sen University, Zhuhai 519082, People's Republic of China
[12] Dipartimento di Fisica, Università di Padova, 35131 Padova, Italy
[13] Sibley School of Mechanical and Aerospace Engineering, Cornell University, Ithaca, NY 14850, USA
[14] Instituto de Astrofisica de Andalucia, CSIC, 18008 Granada, Spain
[15] Depto. Astronomía, Fac. Ciencias, Udelar, Montevideo, Uruguay
[16] Institute of Space Sciences (CSIC/IEEC), c/ Can Magrans, s/n, 08193 Cerdanyola del Vallés (Barcelona), Catalonia, Spain
[17] Department of Physics, Aristotle University of Thessaloniki, GR 54124 Thessaloniki, Greece
[18] German Aerospace Center, DLR, 51147 Cologne, Germany
[19] School of Aeronautic Science and Engineering, Beihang University, Beijing 100191, People's Republic of China
[20] Department of Climate and Space Sciences and Engineering, University of Michigan, Ann Arbor, MI 48109, USA
[21] Johns Hopkins University Applied Physics Laboratory, Laurel, MD 20723, USA
[22] Instituto de Fisica Aplicada a las Ciencias y las Tecnologias, Universidad de Alicante, 03080 Alicante, Spain
[23] Université Côte d'Azur, Observatoire de la Côte d'Azur, CNRS, Laboratoire Lagrange, Nice F-06304, France
Received 2025 January 17; revised 2025 June 10; accepted 2025 June 26; published 2025 July 23

Abstract

The successful impact of the Double Asteroid Redirection Test (DART) spacecraft on Dimorphos enabled the first-ever extensive observation of a postimpact ejecta tail from a binary asteroid system. Studying the ejecta can provide insights into impact physics and asteroid composition and inform future asteroid missions. In this research, the orbital capture of the impact ejecta around the Didymos binary asteroid system is investigated. The ejecta dynamics are described using an augmented bicircular restricted four-body model, which incorporates the binary's irregular gravity field and solar radiation pressure (SRP) acceleration. Typical periodic orbit (PO) families, including planar Lyapunov and terminator orbits, are selected as the candidates for capture analysis. The candidate POs are perturbed and backward-propagated using the invariant manifold theory, and eligible trajectories intersecting the asteroids' surfaces are recorded. The ejecta characteristics of different POs are summarized from three principal aspects: ejection location, ejection velocity, and ejection angle. The influence of two critical factors is qualitatively assessed, including the geometry of the asteroids in the binary system and the strength of SRP acceleration. Lastly, the likelihood for the ejecta from the DART impact being transferred to candidate POs is assessed.

Unified Astronomy Thesaurus concepts: Asteroids (72); Asteroid dynamics (2210); Ejecta (453); Astronomical simulations (1857)

1. Introduction

On 2022 September 26, NASA's Double Asteroid Redirection Test (DART) spacecraft intentionally impacted Dimorphos, a small moonlet orbiting the larger asteroid Didymos in the binary asteroid system (A. F. Cheng et al. 2023). The impact successfully reduced the binary orbit period by 33.0 ± 1.0 minutes, demonstrating the feasibility of using kinetic impacts to deflect potentially hazardous asteroids (C. A. Thomas et al. 2023). In the aftermath of the DART impact, the resulting ejecta features, including ejecta cloud and ejecta tails, were observed by telescopes worldwide over several weeks (J.-Y. Li et al. 2023). Detailed analysis of the ejecta and its dynamics provides crucial insights into the asteroid's composition (S. Raducan et al. 2024), the momentum transfer from the kinetic impact (A. F. Cheng et al. 2023), and the characterization and distribution of ejected materials (A. Graykowski et al. 2023; F. Moreno et al. 2023). Furthermore, studying ejecta mechanics can benefit the development of planetary defense strategies and enhance the safety of future asteroid missions (N. L. Chabot et al. 2024).

The dynamics of ejecta and its evolution has been extensively investigated in previous research. A detailed

Table 1
Selected Properties of the Didymos System before and after the DART Impact

	Preimpact	Postimpact
Total mass of the system[a] (10^{11} kg)	5.3 ± 0.2	Assumed unchanged
Bulk density of Didymos, Dimorphos[b] (kg m^{-3})	2790 ± 140, 2400 ± 300	Assumed unchanged
Mean separation of component centers[c] (km)	1.189 ± 0.017	1.152 ± 0.018
Mutual orbital period[d] (hr)	11.921493 ± 0.000016	11.3674 ± 0.0004
Mutual orbital eccentricity[e]	<0.03	0.0274 ± 0.0015
Didymos rotation period[f] (hr)	2.2600 ± 0.0001	Assumed unchanged
Dimorphos rotation period[g] (hr)	11.921493 ± 0.000016	Pending
Geometric albedo[h]	0.15 ± 0.02	Assumed unchanged

Notes.
[a] Preimpact value from S. P. Naidu et al. (2024).
[b] Preimpact values from S. P. Naidu et al. (2024) for Didymos and R. T. Daly et al. (2023) for Dimorphos.
[c] Preimpact value from S. P. Naidu et al. (2024); postimpact change in value from A. J. Meyer et al. (2023).
[d] Pre- and postimpact values from S. P. Naidu et al. (2024).
[e] Preimpact value from P. Scheirich & P. Pravec (2009); postimpact value from S. P. Naidu et al. (2024).
[f] Preimpact value from P. Pravec et al. (2006).
[g] Preimpact value assumed to be the same as Dimorphos orbital period (tidal lock).
[h] Preimpact value from R. T. Daly et al. (2023).

dynamical model incorporating all relevant forces is presented by Y. Yu et al. (2017) to simulate the evolution of a postimpact ejecta cloud from the Didymos binary system. A. Rossi et al. (2022) simulate the dynamical evolution of DART ejecta particles over various timescales and analyze their survivability within the chaotic dynamical environment. Similarly, F. Ferrari et al. (2022) investigate the same impact scenario and offer a more comprehensive multiphase analysis. In their work, the early collision phase is simulated with an *N*-body granular model, and the following ballistic phase is simulated with an *N*-body high-fidelity propagator. In the work of E. Peña-Asensio et al. (2024), a simulation is conducted to analyze the dynamical evolution of 3 million DART ejecta particles across three size populations, tracking their trajectories over time to determine whether any could potentially reach Mars or the Earth–Moon system in the future. Comparable studies have also been conducted for previous asteroid missions. For instance, S. Soldini et al. (2022) examine the evolution of ejecta particles resulting from the artificial impact of the Hayabusa2 spacecraft on Ryugu and estimate the probability of particle-induced damage. L. Chappaz et al. (2013) explore the ejecta evolution from Mars's surface, suggesting that certain materials on Phobos and Deimos are likely to be transferred through Mars surface impacts. P. Gavin et al. (2013) use Autodyn simulation to understand more about the relationship between impact ejecta and the formation mechanism of the clay minerals on Mars. Additionally, D. J. Scheeres et al. (2002) conduct an extensive review on the perturbations influencing ejecta dynamics, offer a classification of trajectories of lofted ejecta, and summarize the possible fates of ejecta particles.

It is noteworthy that, in the majority of research on ejecta dynamics, the standard approach involves modeling the ejecta cone and analyzing the ejecta evolution by forward-propagating from the predefined initial conditions generated from the ejecta cone. D. Villegas-Pinto et al. (2020), however, propose an alternative methodology that reverses the standard process. In their work, they first identify target periodic orbits (POs) and then determine the ejection conditions required for the ejecta to reach these orbits. Building on their method, this study adopts a similar reverse approach to identify ejection conditions facilitating ejecta transfer to candidate POs within the Didymos binary asteroid system. Unlike the previous study, our work utilizes a more complex model that accounts for the asteroids' irregular gravitational fields and the intricate geometry of the binary system. This refined modeling framework is designed to enhance the fidelity of ejecta motion simulations in the vicinity of the binary system, aiming to provide meaningful insights that could be valuable for ESA's Hera mission (P. Michel et al. 2022), which will conduct a detailed postimpact survey of the system in the near future.

This paper is organized as follows. The necessary physical and orbital parameters of the Didymos binary system are presented first, followed by an analysis of the critical acceleration and perturbations. Subsequently, the augmented bicircular restricted four-body (BCRFB) dynamics including the polyhedron asteroid's gravity and cannonball solar radiation pressure (SRP) model is detailed. In the following section, candidate POs are provided, and the ejecta orbital capture methodology based on the invariant manifold theory is introduced. Additionally, the detailed algorithm based on backward propagation is provided. The simulation results are summarized in terms of the candidate POs, and the implications of this research for the Hera mission are discussed. Conclusions are drawn in the last section of this paper.

2. The Didymos Binary System

In this section, the physical characteristics and orbital properties of the Didymos binary system are introduced. Then the dynamical environment in the vicinity of the binary system is discussed, with the critical acceleration sources being analyzed.

2.1. Physical and Orbital Properties

The physical and orbital properties of Didymos and Dimorphos necessary for this research are summarized in Tables 1 and 2, with data sources provided in the table footnotes. Note that the "preimpact" and "postimpact" values are from just prior to and just after the DART impact, respectively. The values in Table 1 are based on the latest measurements and modeling available at the time of this

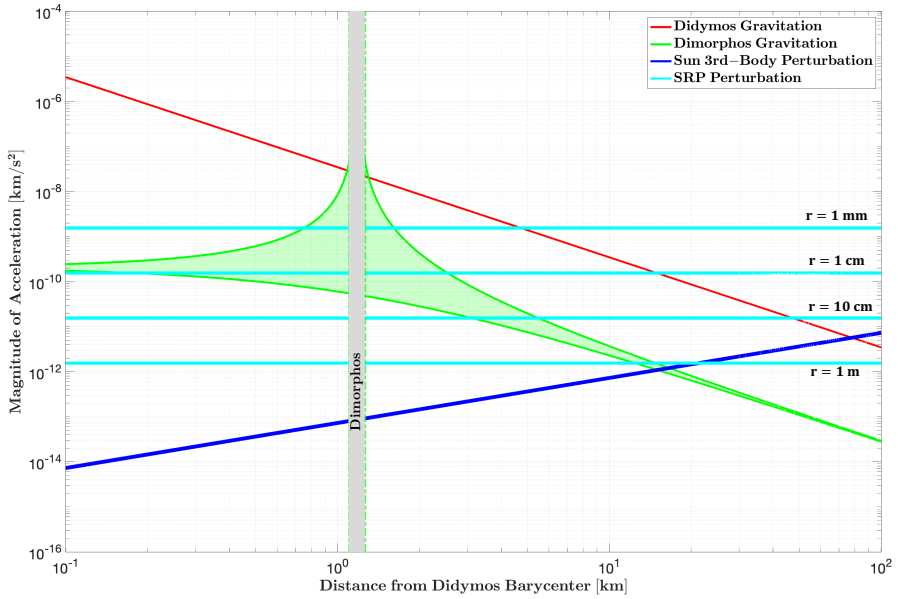

Figure 1. Acceleration environment in the vicinity of the Didymos binary system. The *x*-axis indicates the radial distance along the line extending from the Didymos barycenter toward the Dimorphos barycenter. The ranges between minimum and maximum accelerations caused by the gravitation of homogeneous spherical Didymos and Dimorphos, third-body gravitational perturbation from the Sun, and SRP on spherical ejecta of varying radii are presented. These ranges are calculated over a time frame spanning from the DART impact on 2022 September 26 to 60 days postimpact. During the investigated period, the Sun–Didymos distance remains relatively stable, with a maximum variation of 3.16%. Therefore, the minimum and maximum perturbing accelerations from the Sun are on the same order of magnitude, leading to an almost invisible blue shaded area in the figure.

writing, with most being consistent with those reported by S. P. Naidu et al. (2024) and D. C. Richardson et al. (2024). The orbital properties of Didymos are retrieved from the small-body database of Jet Propulsion Laboratory (2024) and presented in Table 2. The osculating orbital elements of Didymos are defined in the heliocentric inertial frame, while those of Dimorphos are defined with respect to the binary's orbit. Although slight variations in the orbital period and semimajor axis were observed for Dimorphos after the DART impact, its postimpact orbit remains nearly circular. In this research, the postimpact orbital parameters are applied. Additionally, to accurately model the gravity field of both asteroids, the up-to-date shape models of Didymos and Dimorphos, *Didyv003.obj* and *Dimov004.obj*, are utilized. Both shape models are derived from DRACO and LICIACube images and enable a polyhedron representation of the two asteroids for accurate gravity field calculation (R. T. Daly et al. 2024). Based on the latest shape models, the bulk density of the two asteroids has been adjusted in this research, resulting in a slight deviation from the reference values reported in Table 1, though still within their 1σ uncertainty range.

2.2. Dynamical Environment

The dynamical environment is crucial when analyzing the ejecta's impact and evolution around the Didymos binary system. Figure 1 presents the major acceleration contributions related to the ejecta dynamics, plotted as a function of distance along the line directed from the Didymos barycenter toward the Dimorphos barycenter. The figure shows the ranges between minimum and maximum accelerations due to (1) the gravitation of homogeneous spherical Didymos and Dimorphos, (2) third-body gravitational perturbation of the Sun, and (3) the SRP acceleration on spherical ejecta of different radii, all within a time span of 60 days following the

Table 2
Orbital Characteristics of Didymos[a]

Parameter	Value
Sidereal orbital period (days)	768.9463824157542 ± 2.0827e-7
Semimajor axis (au)	1.6425997566424 ± 2.9659e-10
Eccentricity	0.3832511742413838 ± 1.2777e-10
Inclination to the ecliptic (deg)	3.41417645416608 ± 1.6187e-8
Longitude of ascending node (deg)	72.9859763839095 ± 2.2208e-7
Argument of perihelion (deg)	319.602659066438 ± 2.5006e-7

Note.
[a] Values from the small-body database of Jet Propulsion Laboratory (2024).

DART impact on 2022 September 26. As depicted in Figure 1, within a 10 km distance, the gravitation of Didymos and Dimorphos remains the dominant force acting on the ejecta. The green colored region, which corresponds to Dimorphos's acceleration, arises from the binary's relative motion about the system's barycenter. As the distance from the Didymos barycenter increases, the perturbation of solar gravity gradually becomes more significant. Since the perihelion of Didymos's orbit was reached on 2022 October 22, during the investigated period, the Sun–Didymos distance remains relatively stable, with a maximum variation of 3.16%. Therefore, the minimum and maximum perturbing accelerations from the Sun are on the same order of magnitude, leading to an almost invisible blue shaded area in the figure. Similarly, the variation in the SRP acceleration for each ejecta size is also not noticeable graphically. However, in this low-gravity environment, the SRP acceleration becomes comparable to the aforementioned gravitational attraction, particularly for smaller ejecta, which are more susceptible to its influence. Such a fact necessitates the incorporation of the SRP acceleration, alongside the other dominant gravitation in the modeling of ejecta dynamics. Note that the collisional and

gravitational interactions between the ejecta particles are not considered in this research.

3. Ejecta Dynamics

In this section, the cannonball model and polyhedron model are introduced to model the SRP acceleration and the asteroids' gravity field, respectively. Subsequently, an augmented BCRFB model and an augmented circular restricted three-body problem (CRTBP) are detailed for the modeling of the ejecta dynamics.

3.1. Cannonball Model of SRP

To approximate the SRP acceleration acting on a spherical ejecta around the binary system, the cannonball model is adopted (D. J. Scheeres 2016). This model assumes a constant projected area and homogeneous physical properties (e.g., reflectivity) for the object of interest. The SRP acceleration of an ejecta derived from the cannonball model is expressed as

$$\boldsymbol{a}_{\mathrm{SRP}} = -\frac{P_{\mathrm{SRP}} C_r}{m/A} \frac{(\boldsymbol{d}-\boldsymbol{r})}{|\boldsymbol{d}-\boldsymbol{r}|}, \tag{1}$$

where $\boldsymbol{d}$ is the vector from an asteroid to the Sun and $\boldsymbol{r}$ is the vector from the asteroid's barycenter to the ejecta. C_r represents the ejecta's reflectivity coefficient, which is associated with the asteroid's albedo ρ_s by the relationship $C_r = 1 + \rho_s$. A is the ejecta's projected area, and m is the ejecta's mass. The SRP exerted on the ejecta P_{SRP} at the distance of $|\boldsymbol{d}-\boldsymbol{r}|$ is defined by (D. A. Vallado 2001)

$$P_{\mathrm{SRP}} = \frac{S_0}{c}\left(\frac{d_0}{|\boldsymbol{d}-\boldsymbol{r}|}\right)^2, \tag{2}$$

where $S_0 = 1367\ \mathrm{W\ m^{-2}}$ is the solar flux at 1 au, c is the speed of light, and $d_0 = 1$ au is the Sun–Earth mean distance. In the vicinity of an asteroid, where the condition $|\boldsymbol{r}| \ll |\boldsymbol{d}|$ is satisfied, the SRP acceleration in Equation (1) can be approximated by

$$\boldsymbol{a}_{\mathrm{SRP}} = -\frac{P_{\mathrm{SRP}} C_r}{m/A} \frac{\boldsymbol{d}}{|\boldsymbol{d}|}. \tag{3}$$

According to Equation (3), the SRP acceleration acting on an ejecta maintains a constant magnitude and is consistently oriented along the Sun–asteroid line. Note that the eclipsing effects on the SRP are not considered in this study.

3.2. Polyhedron Model of Asteroid Gravitation

The polyhedron model is a numerical approach used to represent the gravitational field of a small irregular celestial body in its body-fixed frame. This method approximates the shape of such bodies by employing a polyhedron composed of planar triangular facets, which allows for an accurate calculation of the body's gravitational field. In this work, the algorithm proposed by R. A. Werner & D. J. Scheeres (1996) is employed, which provides the closed-form expressions for the exterior gravitation due to a constant-density polyhedron. The gravitational potential U_{poly}, gravitational force ∇U_{poly}, and Laplacian $\nabla^2 U_{\mathrm{poly}}$ of a constant-density polyhedron utilized in this research are provided in Equation (4a) (R. A. Werner & D. J. Scheeres 1996):

$$U_{\mathrm{poly}} = \frac{1}{2} G\sigma \sum_{e=1}^{n_e} \boldsymbol{r}_e \cdot \boldsymbol{E}_e \cdot \boldsymbol{r}_e \cdot L_e - \frac{1}{2} G\sigma \sum_{f=1}^{n_f} \boldsymbol{r}_f \cdot \boldsymbol{F}_f \cdot \boldsymbol{r}_f \cdot \omega_f, \tag{4a}$$

$$\nabla U_{\mathrm{poly}} = -G\sigma \sum_{e=1}^{n_e} \boldsymbol{E}_e \cdot \boldsymbol{r}_e \cdot L_e + G\sigma \sum_{f=1}^{n_f} \boldsymbol{F}_f \cdot \boldsymbol{r}_f \cdot \omega_f, \tag{4b}$$

$$\nabla^2 U_{\mathrm{poly}} = -G\sigma \sum_{f=1}^{n_f} \omega_f = \begin{cases} 0 & \text{outside the body} \\ -4\pi G\sigma & \text{inside the body} \end{cases}, \tag{4c}$$

where G is the gravitational constant and σ is the celestial body's density. n_e and n_f denote the number of edges and faces of the polyhedron, respectively. $\boldsymbol{r}_e$ represents the vector from an external point to any point on an edge e, and $\boldsymbol{r}_f$ represents the vector from an external point to any point in a face f. $\boldsymbol{E}_e$ and $\boldsymbol{F}_f$ are dyads defined by the normal vectors of an edge e and a face f. L_e and ω_f are integration factors related to an edge e and a face f, respectively. The expressions of $\boldsymbol{E}_e$, $\boldsymbol{F}_f$, L_e, and ω_f are provided in the relevant references (X. Fu et al. 2024). Note that the Laplacian $\nabla^2 U_{\mathrm{poly}}$ in Equation (4c) can perform as a sensitive indicator for determining whether a point lies inside or outside the polyhedron. This property is utilized in the subsequent section to design the orbital capture methodology.

3.3. Augmented BCRFB Model

According to the acceleration magnitude analysis in Section 2.2, the gravitation of the Sun, Didymos, and Dimorphos, along with the SRP acceleration, significantly influences the ejecta's motion near the binary system. To account for these influences, an augmented BCRFB model is introduced to describe the ejecta dynamics. Note that although the heliocentric orbit of the Didymos binary system is characterized by an eccentricity of approximately 0.38, for an analysis window of 60 days after the DART impact, the circular approximation holds adequately accurate for capturing the key dynamical features relevant to ejecta motion, as discussed in Section 2.2.

As illustrated in Figure 2, in this model, the motion of a mass particle m_4 is governed by the SRP perturbation and the gravitational fields of three primary masses m_1, m_2, and m_3, with their masses satisfying the relationship $m_1 \gg m_2 \gg m_3$. Additionally, m_2 and m_3 are in circular motion about their barycenter with a mutual separation of d_2, while m_1 and m_2–m_3 orbit their common center of mass with a radius d_1. It is noteworthy that when excluding the influence from the SRP, the bicircular model has been extensively applied to model the Sun–Earth–Moon system. This model has been shown to replicate the qualitative behavior of the real system within certain regions of phase space (W. S. Koon et al. 2000). Consequently, it has been effectively employed to systematically explore low-energy lunar transfer trajectories (J. S. Parker & R. L. Anderson 2014).

Based on the augmented BCRFB model, the motion of ejecta in the vicinity of the Didymos binary system is investigated in a Didymos-centered synodic frame, denoted by $\{\boldsymbol{x}\}_{D_1}^{\mathrm{syn}}$. As shown in Figure 3, in this reference frame, the barycenters of the Sun (denoted by S) and Didymos (denoted by D_1) remain stationary, while Dimorphos (denoted by D_2)

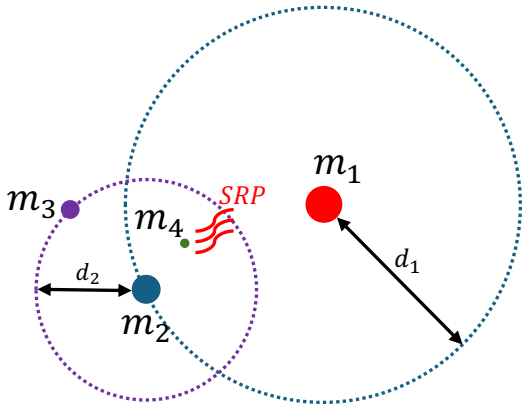

Figure 2. Illustration of the augmented BCRFB model. In this model, the motion of a mass particle m_4 is governed by the SRP perturbation and the gravitational fields of three primary masses m_1, m_2, and m_3, with their masses satisfying the relationship $m_1 \gg m_2 \gg m_3$. Additionally, m_2 and m_3 are in circular motion about their barycenter with a mutual separation of d_2, while m_1 and m_2–m_3 orbit their common center of mass with a radius d_1.

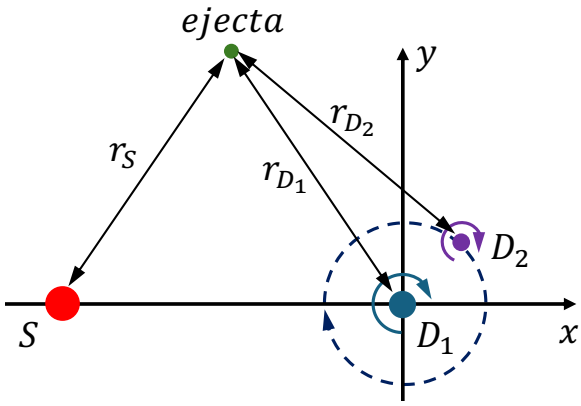

Figure 3. Didymos-centered synodic frame of the augmented BCRFB model for the Sun–Didymos–Dimorphos system. In this reference frame, the barycenters of the Sun (denoted by S) and Didymos (denoted by D_1) remain stationary, while Dimorphos (denoted by D_2) rotates clockwise about the origin. Furthermore, both Didymos and Dimorphos are approximated as polyhedrons and rotate clockwise about their respective major principal axes.

rotates clockwise about the origin. Furthermore, both Didymos and Dimorphos are approximated as polyhedrons and rotate clockwise about their respective major principal axes. Given the fixed positions of the Sun and Didymos, the SRP acceleration in Equation (3) can be approximated as acting along the $+x$ direction. To simplify the derivation of the dynamics in $\{\boldsymbol{x}\}_{D_1}^{\mathrm{syn}}$, the following normalized units are utilized: the unit of mass is defined as the total mass of the three primary bodies, the unit of length is selected as the average Sun–Didymos distance over a 60 day period following the DART impact, and the unit of time is chosen such that the orbital period of a heliocentric circular orbit, with a radius equal to the selected unit of length, is 2π. By means of the normalization above, the equations of motion (EOMs) for the augmented BCRFB model in the synodic frame $\{\boldsymbol{x}\}_{D_1}^{\mathrm{syn}}$ can be expressed as

$$\begin{cases} \ddot{x} - 2\dot{y} = (x + \mu_S) - \dfrac{\mu_S(x+1)}{r_S^3} + a_{\mathrm{poly}}^{D1}|_x + a_{\mathrm{poly}}^{D2}|_x + \beta \\ \ddot{y} + 2\dot{x} = y - \dfrac{\mu_S\, y}{r_S^3} + a_{\mathrm{poly}}^{D1}|_y + a_{\mathrm{poly}}^{D2}|_y \\ \ddot{z} = -\dfrac{\mu_S\, z}{r_S^3} + a_{\mathrm{poly}}^{D1}|_z + a_{\mathrm{poly}}^{D2}|_z \end{cases}, \tag{5}$$

where μ_S denotes the Sun's normalized mass, r_S denotes the Sun–ejecta distance, and β is the normalized SRP acceleration. The polyhedral gravitational accelerations of Didymos and Dimorphos in the synodic frame are denoted as $\boldsymbol{a}_{\mathrm{poly}}^{D1}$ and $\boldsymbol{a}_{\mathrm{poly}}^{D2}$, respectively. Such a denotation is adopted to distinguish it from the ∇U_{poly} in Equation (4b), as the gravitational terms of a polyhedron model are typically derived in an asteroid body-fixed frame. The coordinate transformation between the asteroid body-fixed frame and the synodic frame is provided in the following section. Additionally, to rigorously adhere to the definition of the augmented BCRFB model and derive the EOMs above, the origin of the synodic frame should be placed at the binary system's barycenter. However, given that 99.2% of the system's mass is concentrated in Didymos, the barycenter of the binary system is located approximately 10 m away from Didymos's barycenter. Thus, for simplification, we assume that the binary system's barycenter coincides with the barycenter of Didymos. Note that in the augmented BCRFB model, Dimorphos is assumed to be in principal axis rotation, a state that has likely changed following the DART impact (D. C. Richardson et al. 2024). If Hera's future observations confirm the evidence of tumbling or complex rotational states of Dimorphos, the ejecta dynamics need to be reformulated in a generalized noninertial frame or by integrating in an inertial frame with a time-dependent shape and attitude model of the asteroid.

3.4. Augmented CRTBP

It is noteworthy that, by replacing the self-rotating Didymos and Dimorphos in Figure 3 with a single point mass representing their total mass while keeping the remaining configurations unchanged, this substitution is equivalent to replacing the polyhedral accelerations of Didymos and Dimorphos in Equation (5) with the gravitational acceleration of the point mass. Consequently, the corresponding EOMs turn into

$$\begin{cases} \ddot{x} - 2\dot{y} = (x + \mu_S) - \frac{\mu_S(x+1)}{r_S^3} - \frac{\mu_{DD}x}{r_{DD}^3} + \beta \\ \ddot{y} + 2\dot{x} = y - \frac{\mu_S y}{r_S^3} - \frac{\mu_{DD}x}{r_{DD}^3} \\ \ddot{z} = -\frac{\mu_S z}{r_S^3} - \frac{\mu_{DD}x}{r_{DD}^3} \end{cases}, \tag{6}$$

where μ_{DD} denotes the normalized mass of the point mass and satisfies $\mu_{DD} + \mu_S = 1$. r_{DD} denotes the distance between the point mass and an ejecta particle. Considering the Sun as the primary mass and the combined mass of Didymos and Dimorphos as the secondary, Equation (6) represents the EOMs of the augmented CRTBP defined in a secondary-centered synodic frame. Coherence can be observed between the two models in both their definitions and corresponding EOMs. Furthermore, this model is a generalization from which the augmented Hill problem is derived (S. B. Broschart et al. 2014; D. J. Scheeres 2016). As an autonomous system, Equation (6) admits an energy integral, $\mathcal{C}$, commonly referred

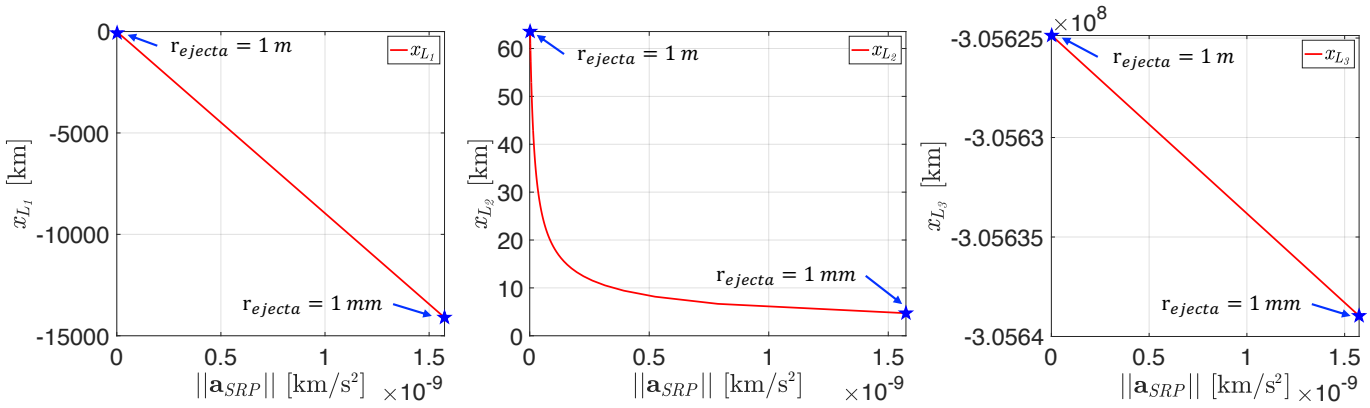

Figure 4. The variation of the x-coordinates of the collinear EPs in the augmented Sun–Didymos and Dimorphos system with respect to the SRP acceleration magnitude $||\boldsymbol{a}_{\rm SRP}||$. The locations of EPs are represented in the synodic frame centered on the secondary, which coincides with the origin of this frame.

Table 3
The SRP Acceleration, Corresponding β, and x-coordinates of EPs for Spherical Ejecta of Different Sizes

$r_{\rm ejecta}$	1 m	10 cm	1 cm	1 mm
$\|\|\boldsymbol{a}_{\rm SRP}\|\|$ (km s^{-2})	$1.5739595 \times 10^{-12}$	$1.5739595 \times 10^{-11}$	$1.5739595 \times 10^{-10}$	1.5739595×10^{-9}
β [−]	2.7686650×10^{-7}	2.7686650×10^{-6}	2.7686650×10^{-5}	2.7686650×10^{-4}
x_{L_1} (km)	-7.2977165×10^{1}	-1.5421298×10^{2}	-1.4104327×10^{3}	-1.4101581×10^{4}
x_{L_2} (km)	6.3545396×10^{1}	4.1451645×10^{1}	1.4832832×10^{1}	4.714368×10^{0}
x_{L_3} (km)	-3.0562487×10^{8}	-3.0562500×10^{8}	-3.0562627×10^{8}	-3.0563896×10^{8}

Note. The symbol [−] indicates that the quantity is dimensionless.

to as the Jacobi constant,

$$\mathcal{C} = -2\tilde{U} - (\dot{x}^2 + \dot{y}^2 + \dot{z}^2), \tag{7}$$

where $\tilde{U} = -\frac{1}{2}[(x + \mu_S)^2 + y^2] - \mu_S/r_S - \mu_{DD}/r_{DD} - \beta x$ is the effective potential.

As expressed in Equation (6), the dynamics of the augmented CRTBP model is governed by two independent parameters, the mass parameter of the secondary μ and normalized SRP acceleration β. Due to the influence of SRP, there are only three collinear equilibrium points (EPs), L_1, L_2, and L_3, in this system (D. J. Scheeres & F. Marzari 2002). The equilateral EPs in the CRTBP, L_4 and L_5, disappear when β is nonzero, since the original balance is disrupted by the SRP acceleration along the x-direction. Additionally, the magnitude of SRP acceleration significantly affects the locations of collinear EPs, especially when the mass parameter μ is relatively larger (S. Soldini et al. 2020).

In this research, for the Sun–Didymos and Dimorphos system, the mass parameter μ corresponds to $\mu_{DD} = 2.665 \times 10^{-19}$, and the β value varies with respect to the size of the spherical ejecta. The variation of the x-coordinates of the collinear EPs in the augmented Sun–Didymos and Dimorphos system as a function of the SRP acceleration magnitude $||\boldsymbol{a}_{\rm SRP}||$ is shown in Figure 4. The plotted range of $||\boldsymbol{a}_{\rm SRP}||$ corresponds to spherical ejecta with radii ranging from 1 m to 1 mm. Note that smaller spherical ejecta particles experience greater SRP acceleration. As observed in Figure 4, as $||\boldsymbol{a}_{\rm SRP}||$ (i.e., the β value) increases, the positions of L_1 and L_3 shift further away from the secondary and primary, respectively, whereas L_2 moves closer to the secondary. This phenomenon occurs because, for L_1/L_3, the gravitational attraction from the secondary/primary is compensated by the SRP, allowing L_1/L_3 to shift further outward to balance the centrifugal force. In contrast, for L_2, the secondary's gravitational attraction has to be stronger to offset the SRP, causing L_2 to move closer to the secondary. The SRP acceleration magnitude $||\boldsymbol{a}_{\rm SRP}||$, the corresponding β value, and the EPs' x-coordinates for the spherical ejecta with radii of 1 m, 10 cm, 1 cm, and 1 mm are summarized in Table 3. As shown in Table 3, L_1 and L_2 are no longer symmetric about the secondary due to the influence of SRP.

4. Orbital Capture Methodology

In this section, the methodology of ejecta orbital capture is outlined. Note that in this study, the term "capture" specifically refers to the arrival of an ejecta particle in the vicinity of a PO, originating from the surfaces of Dimorphos and Didymos and facilitated by the manifold-based dynamical process. This usage does not imply permanent gravitational capture but rather a temporary, dynamically induced transition into a localized region of interest. First, the computation and analysis of candidate POs suitable for the ejecta capture are provided. Then, the invariant manifold theory is introduced to enable the orbital capture of ejecta by these POs. Lastly, the algorithm for the capture analysis is presented in detail, accompanied by the corresponding pseudocode for implementation.

4.1. POs for Orbital Capture

POs play an important role in understanding the dynamical environment around an asteroid and are commonly applied as scientific orbits in various asteroid missions. Investigating whether ejecta can remain in certain POs over both short and extended periods is essential for facilitating future sampling missions and informing the design of optimal scientific trajectories.

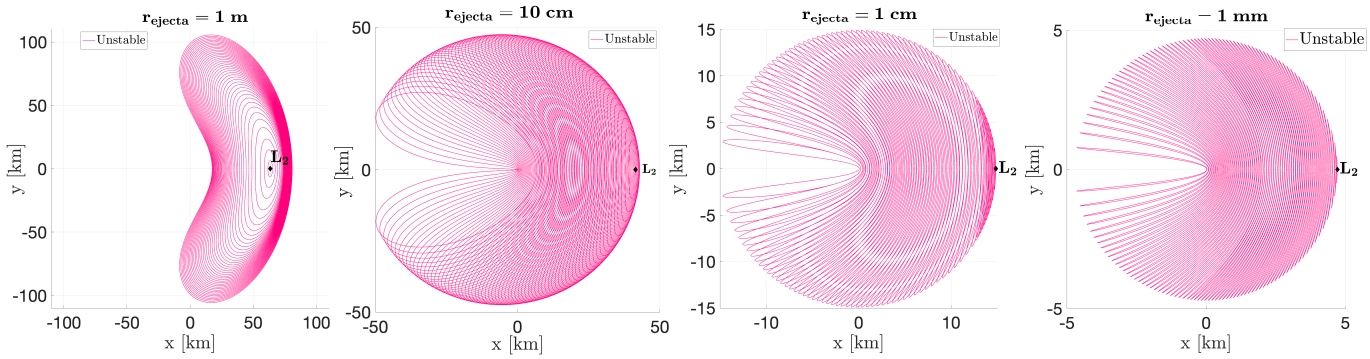

Figure 5. Planar Lyapunov orbits originating from L_2 in the augmented Sun–Didymos and Dimorphos CRTBP model for spherical ejecta with different radii. The combined mass of Didymos and Dimorphos is located at the origin of the secondary-centered synodic frame. From left to right, the subplots correspond to ejecta radii of 1 m, 10 cm, 1 cm, and 1 mm. Note that a smaller ejecta radius corresponds to a higher SRP acceleration of the ejecta.

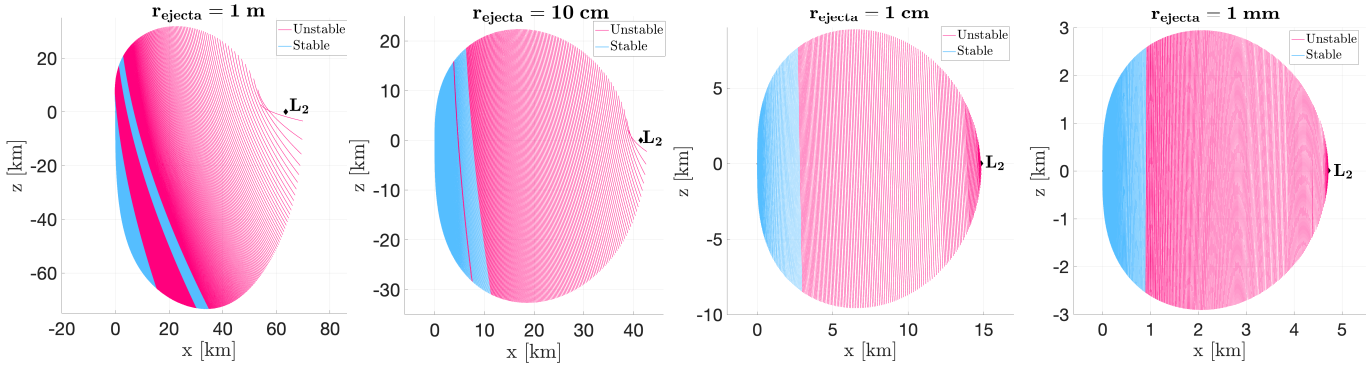

Figure 6. Terminator orbits originating from L_2 in the augmented CRTBP model for spherical ejecta with different radii. The combined mass of Didymos and Dimorphos is located at the origin of the secondary-centered synodic frame. From left to right, the subplots correspond to ejecta radii of 1 m, 10 cm, 1 cm, and 1 mm. Note that a smaller ejecta radius corresponds to a higher SRP acceleration of the ejecta.

To generate the natural POs around the Didymos binary system, the dynamics of the augmented CRTBP model in Section 3.4 is employed. This model represents the autonomous system that most closely approximates the ejecta dynamics established in the augmented BCRFB model. A predictor–corrector scheme based on the pseudo-arclength continuation method (X. Fu et al. 2024) is utilized to compute PO families in the augmented CRTBP model. The linear stability of a PO is assessed using the stability indices (X. Fu et al. 2022), which are derived from its monodromy matrix $\Phi(T)$, i.e., the state transition matrix integrated over one orbital period T for the PO.

Based on the aforementioned methods, two specific PO families in the augmented CRTBP model are selected and computed to investigate the ejecta orbital capture: the L_2 planar Lyapunov orbit family and terminator orbit family. The two families are illustrated in Figures 5 and 6, respectively. In each case, the SRP acceleration acting on the spherical ejecta of the varying sizes defined in Table 3 is considered individually. The corresponding orbit families are presented separately, with their orbital periods summarized in Table 4. As shown in Figure 5, the planar Lyapunov orbit family emerges from L_2 and progressively approaches the secondary. As the SRP acceleration increases, the maximum amplitude of the planar Lyapunov orbit family decreases. A similar decreasing trend is observed in the family's orbital period, shrinking from approximately 150 to 3 days. It is noteworthy that the planar Lyapunov family remains entirely linearly unstable.

Table 4
Orbital Periods of Planar Lyapunov and Terminator PO Families in the Augmented CRTBP Model

r_{ejecta}	1 m	10 cm	1 cm	1 mm
$T_{Lyapunov}$ (days)	[169.23, 229.22]	[85.86, 98.91]	[12.15, 22.16]	[2.15, 3.98]
$T_{terminator}$ (days)	(0, 171.17]	(0, 98.75]	(0, 22.15]	(0, 3.98]

In contrast to the planar Lyapunov orbit, the terminator orbits are spatial. These orbits typically reside in the vicinity of the secondary and can serve as transfer gateways or reimpact channels for SRP-sensitive ejecta, such as small dust grains originating from the asteroid surface. The terminator family derives its name from its close proximity to the Sun–terminator plane, i.e., the plane passing through the asteroid's barycenter and perpendicular to the Sun–asteroid line (D. J. Scheeres 2016). The geometry of the SRP vector, which is typically assumed to be constant in direction in a synodic frame, plays a critical role in shaping this family. For instance, when the Sun lies along the negative x-axis in the synodic frame, terminator orbits often align near the plane perpendicular to the SRP direction. Dynamically, these orbits can be interpreted as SRP-modified analogs of classical halo orbits in the CRTBP, with their structure and stability strongly influenced by the direction and magnitude of SRP. As illustrated in Figure 6, the terminator family originates in the vicinity of L_2 and ultimately converges around the secondary.

Similar to the planar Lyapunov family, the terminator family exhibits a reduction in both its maximum amplitude and orbital period as the SRP strengthens. During the continuation process, a terminator orbit can approach the secondary body asymptotically, with its orbital period tending toward 0. Additionally, the family's inclination with respect to the terminator plane decreases as the SRP intensifies. Unlike the entirely unstable planar Lyapunov family, the terminator orbit family includes linearly stable members (depicted as blue orbits in Figure 6) that are located near the secondary. Furthermore, the proportion of linearly stable terminator orbits increases when the SRP strengthens.

The selection of L_2 planar Lyapunov and terminator families stems from their natural evolution toward the secondary as the SRP magnitude increases. Notably, both the Hayabusa2 and DART missions targeted impact sites near the ecliptic plane (S. Watanabe et al. 2019; A. F. Cheng et al. 2023), which further supports the choice of the planar Lyapunov family. Regarding the terminator family, its robustness against the SRP acceleration and uncertainties in an asteroid's dynamical environment have been reported in previous research (D. J. Scheeres 2012). This fact suggests that ejecta captured within this family could pose potential risks to ongoing asteroid missions. Furthermore, both families originate from the L_2 EP, which serves as a gateway for the reimpacting, orbiting, and escaping trajectories in the augmented CRTBP model (D. Villegas-Pinto et al. 2020). Analyzing the POs around this collinear EP can thus provide deeper insight into the likelihood of ejecta escaping or reimpacting the asteroids.

4.2. Invariant Manifold

To effectively build the transfer of the ejecta from an asteroid surface to the candidate POs, the invariant manifold theory (W. S. Koon et al. 2000) is employed to identify feasible transfer trajectories. An invariant manifold is a topological manifold that is invariant under the action of a dynamical system (M. W. Hirsch et al. 1970). The invariant manifolds of a PO contain the set of trajectories that asymptotically approach or depart from the PO in a dynamical system. For a typical linearly unstable PO in a Hamiltonian system, two fundamental types of invariant manifolds are associated with the orbit: the stable and unstable manifolds. The stable manifold comprises trajectories that asymptotically converge to the PO as time advances. In contrast, the unstable manifold consists of trajectories that asymptotically approach the PO in reverse time, i.e., diverging from it as time progresses. Figure 7 illustrates the stable and unstable manifolds of an L_2 planar Lyapunov orbit under the influence of SRP corresponding to the third column of Table 3. Both manifolds emerge from the candidate orbit and intersect with a secondary-centered sphere of 4 km radius. This example demonstrates how an eligible ejecta transfer can be readily established between the central asteroid and the candidate orbit via its manifolds. Note that the 4 km radius sphere is used here only for demonstration and visualization purposes. It does not correspond to the actual physical size of the Didymos–Dimorphos system and is unrelated to the ejecta simulation analysis presented in the following section. Although the shape of the manifolds can change with respect to different β values, the general direction toward the secondary remains unchanged, and the likelihood always exists for the manifolds to reach the close vicinity of the origin. Additionally, since this research focuses on the ejecta reaching the candidate POs rather than those departing from them, the stable manifolds are applied in the following analysis. A backward-propagated trajectory along the stable manifold that eventually reaches the asteroid's surface represents a successful orbital capture. In this reverse process, a surface impact corresponds to an ejection event.

The numerical procedures to approximate the stable manifold of a candidate PO (G. Gómez et al. 1993) are summarized as follows. Let the initial state and orbit period of the PO be denoted by $\boldsymbol{X}(0)$ and T, respectively. The state transition matrix $\Phi(t)$ along this PO can be obtained simultaneously with its corresponding state $\boldsymbol{X}(t)$ by integrating the variational equations over the time span of $[0, T]$. The eigenvalues and eigenvectors of the monodromy matrix, $\Phi(T)$, can be calculated numerically. The eigenvectors associated with the eigenvalue pair $\{\lambda, 1/\lambda\}$ (where $\lambda \in \mathbb{R}$, $\lambda > 1$) can be used to approximate the unstable and stable manifolds locally. Let $\boldsymbol{\nu}^s(\boldsymbol{X}(0))$ represent the normalized stable eigenvector associated with eigenvalue $1/\lambda$. It can be transported from state $\boldsymbol{X}(0)$ to $\boldsymbol{X}(t)$ via the following equation:

$$\boldsymbol{\nu}^s(\boldsymbol{X}(t)) = \Phi(t)\boldsymbol{\nu}^s(\boldsymbol{X}(0)). \tag{8}$$

Note that to use $\boldsymbol{\nu}^s(\boldsymbol{X}(t))$ subsequently, it has to be renormalized, since the state transition matrix $\Phi(t)$ does not preserve the vector norm. The initial guess to approximate the stable manifold at $\boldsymbol{X}(t)$ can be achieved by

$$\boldsymbol{X}^s(\boldsymbol{X}(t)) = \boldsymbol{X}(t) - \epsilon\boldsymbol{\nu}^s(\boldsymbol{X}(t)), \tag{9}$$

where ϵ is a scalar representing the displacement from state $\boldsymbol{X}(t)$. For the Sun–Didymos and Dimorphos system, ϵ is set to 10^{-9} in normalized units to guarantee the linear approximation is satisfied (G. Gómez et al. 1993). Additionally, to obtain the stable manifold directing toward the secondary, the initial guess is integrated backward. Trajectories that intersect an asteroid's surface during the backward propagation correspond to ejecta trajectories, each with a specific ejection location, velocity, and angle.

4.3. Ejecta Capture Simulation

The core function for simulating ejecta capture using the stable manifold is elaborated in this section, with the accompanying pseudocode provided in Algorithm 1. For a given PO with initial state $\boldsymbol{X}_0$ and orbit period T, N_{sample} sample points evenly distributed along the PO are selected to generate the initial guesses for approximating the stable manifold. Sample points with a distance from the origin Δd_{origin} shorter than the minimum extension of Didymos are discarded, and the corresponding N_{sample} is updated accordingly. The propagation time t_{end} for each sample point, defined as the time required to either approach the vicinity of the binary asteroid system or impact one of the asteroids' surfaces in the augmented BCRFB model, is estimated in two steps. First, each sample point is backward-integrated under the augmented CRTBP dynamics using a sufficiently large integration time (e.g., $6T$). The augmented CRTBP dynamics is utilized at this stage to reduce the model complexity while still providing a reliable estimation. If the integrated trajectory intersects a 1 km radius sphere centered at the origin, the intersection time t_{inter} is recorded. Subsequently, the actual propagation time t_{end} is defined with a buffer as $t_{\text{end}} = 1.2t_{\text{inter}}$ to ensure that the trajectory fully reaches the asteroids' surface

in the subsequent more accurate simulations, where the impact with either Didymos or Dimorphos is selected as the ordinary differential equation (ODE) event to define a successful orbital capture. Thus far, the preparation for ejecta integration based on the sample points has been completed.

Algorithm 1 Compute invariant manifold for ejecta capture

1: **function**Compute_InvarMani_EjectaCapture$\boldsymbol{X}(0)$, T, N_{sample}, d_{thresh}, d_{far}
2: Generate N_{sample} initial guesses for stable manifold along the PO ▷ See Section (4.2)
3: Calculate Δd_{origin} and update N_{sample}
4: **For** i = 1 To N_{sample} **do**
5: Initialization: $t_{init} = 0$, $\boldsymbol{X}_{init} = \boldsymbol{X}(t)_i$, $flag_{event} = 0$
6: Estimate propagation time t_{end} using augmented CRTBP dynamics with a sufficient large integration time
7: **while** $t_{init} > t_{end}$ **do**
8: **if** $\Delta d_{thresh} > 0$ **or** $flag_{event} == 5$ **then**
9: Propagate backward using augmented CRTBP dynamics with ODE events ▷ See Equation (6)
10: **switch** $flag_{event}$ **do**
11: **case 1**: **break** ▷ Propagation reaches prescribed t_{end}
12: **case 3**: **break** ▷ Propagation reaches d_{far}
13: **case 2**: $t_{init} = t_{event}$, $\boldsymbol{X}_{init} = \boldsymbol{X}_{event}$ ▷ Propagation reaches d_{thresh}
14: **else**
15: Propagate backward using augmented BCRFB dynamics with ODE events ▷ See Equation (5)
16: **switch** $flag_{event}$ **do**
17: **case 4**: **break** ▷ Propagation reaches prescribed t_{end}
18: **case 6**: **break** ▷ Propagation reaches Didymos's surface
19: **case 7**: **break** ▷ Propagation reaches Dimorphos's surface
20: **case 5**: $t_{init} = t_{event}$, $\boldsymbol{X}_{init} = \boldsymbol{X}_{event}$ ▷ Propagation reaches d_{thresh}
21: Calculate ejection angle and ejection velocity in asteroid body-fixed frames ▷ See Equation (6)

The integration of the N_{sample} initial guesses is performed using the Adams–Bashforth–Moulton PECE solver (L. F. Shampine & M. K. Gordon 1975), with seven predefined ODE events $\text{flag}_{\text{event}}$ to capture specific dynamical conditions during the manifold propagation. Additionally, to accelerate the integration, a distance threshold d_{thresh} of 10 km is applied. The distance threshold triggers two ODE events, where the integration switches from the augmented BCRFB dynamics in Equation (5) to the augmented CRTBP dynamics in Equation (6), or vice versa. This approach is supported by the acceleration magnitude analysis in Section 2.2, which demonstrates that the gravitational influence of Didymos and Dimorphos becomes less dominant beyond a 10 km distance. Apart from the two $\text{flag}_{\text{event}}$ corresponding to the d_{thresh}, the remaining five ODE events are designed to terminate the current integration. Specifically, these events occur when the integration reaches a prescribed propagation time t_{end}, the integrated trajectory intersects the surface of Didymos or Dimorphos, or the propagation extends too far from the binary system and reaches the distance $d_{\text{far}} = 600$ km. Note that the intersection of a trajectory with the surface of a polyhedron asteroid can be determined from the Laplacian $\nabla^2 U_{\text{poly}}$ provided in Equation (4c). Additionally, since no interaction is required between the integration of different sample points, the entire process can be readily parallelized to achieve a significant acceleration.

Once the integration of all sample points is completed, the impact states are achieved to be postprocessed for ejection-related information. Since the integration is performed in the Didymos-centered synodic frame, the associated states have to

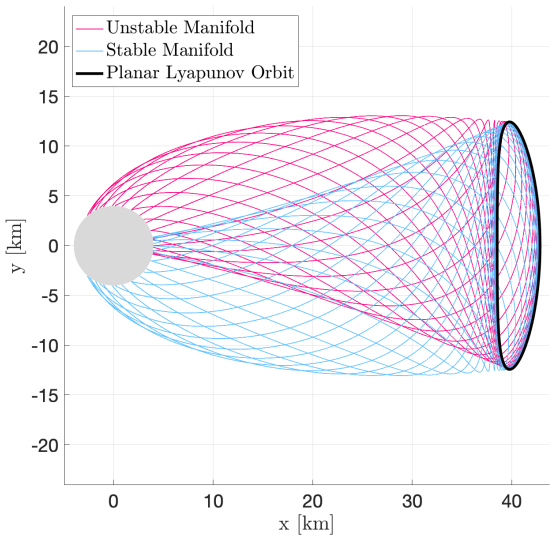

Figure 7. Stable (blue) and unstable (pink) manifolds emerging from an L_2 planar Lyapunov orbit and directing to the secondary. Both manifolds emerge from the candidate orbit and intersect with a secondary-centered sphere of 4 km radius.

be transformed into the Didymos/Dimorphos body-fixed frame to calculate the ejection location, ejection velocity, and ejection angle. For an ejecta departing from the surface of an asteroid modeled as a polyhedron composed of numerous triangular facets, its ejection angle is defined as the angle between the local facet normal and the ejection velocity vector, measured in the asteroid's body-fixed reference frame. Additionally, the transformation is provided as follows. Let $\{\boldsymbol{x}\}_{D_1}^{\text{syn}}$ denote the coordinate of the Didymos-centered synodic frame and $\{\boldsymbol{x}\}_{D_1}^{\text{body}}$ and $\{\boldsymbol{x}\}_{D_2}^{\text{body}}$ denote the coordinates of the Didymos-centered and Dimorphos-centered body-fixed frames, respectively. The transformation from the Didymos-centered synodic frame to the two asteroid-centered body-fixed frames is given as

$$\begin{aligned}\{\boldsymbol{x}\}_{D_1}^{\text{body}} &= [R_{ID_1}][R_{IS}]^{-1}\{\boldsymbol{x}\}_{D_1}^{\text{syn}}\\ \{\boldsymbol{x}\}_{D_2}^{\text{body}} &= [R_{ID_2}]\{[R_{IS}]^{-1}\{\boldsymbol{x}\}_{D_1}^{\text{syn}} - \boldsymbol{a}_{DD}\},\end{aligned} \tag{10}$$

where $\boldsymbol{a}_{DD} = [a_{DD}\cos\theta_{DD}, a_{DD}\sin\theta_{DD}, 0]^T$ is the position vector of Dimorphos in the Didymos-centered inertial frame. Matrix $[R_{IS}]$ represents the transformation from the Didymos-centered inertial frame to the Didymos-centered synodic frame, while matrices $[R_{ID_1}]$ and $[R_{ID_2}]$ represent the transformations from the inertial frame to the body-fixed frames of Didymos and Dimorphos, respectively. Since in the bicircular model, Didymos is rotating counterclockwise around the Sun, and both Didymos and Dimorphos exhibit clockwise self-rotation, the three matrices $[R_{IS}]$, $[R_{ID_1}]$, and $[R_{ID_2}]$ are expressed as

$$\begin{aligned}[R_{IS}] &= \begin{bmatrix}\cos\theta_{SD_1} & \sin\theta_{SD_1} & 0\\ -\sin\theta_{SD_1} & \cos\theta_{SD_1} & 0\\ 0 & 0 & 1\end{bmatrix},\\ [R_{ID_j}] &= \begin{bmatrix}\cos\theta_{D_j} & -\sin\theta_{D_j} & 0\\ -\sin\theta_{D_j} & -\cos\theta_{D_j} & 0\\ 0 & 0 & -1\end{bmatrix},\end{aligned} \tag{11}$$

Table 5
The Ejecta Capture Rate of Planar Lyapunov Orbits and Corresponding Time of Flight

r_{ejecta}	1 m	10 cm	1 cm	1 mm
Didymos	22.91%	41.46%	52.08%	67.71%
$t_{f,\text{min}}$ (days)	149.55	3.57	0.50	0.20
$t_{f,\text{max}}$ (days)	907.81	422.02	91.38	11.93
$t_{f,\text{avr}}$ (days)	253.89	131.06	21.92	2.75
Dimorphos	3.98%	6.64%	8.83%	9.10%
$t_{f,\text{min}}$ (days)	147.82	3.54	0.51	0.18
$t_{f,\text{max}}$ (days)	783.54	374.90	78.65	9.31
$t_{f,\text{avr}}$ (days)	271.11	128.14	19.99	2.43

Table 6
The Ejecta Capture Rate of Terminator Orbits and Corresponding Time of Flight

r_{ejecta}	1 m	10 cm	1 cm	1 mm
Didymos	0.62%	2.19%	5.14%	13.03%
$t_{f,\text{min}}$ (days)	149.88	78.14	17.84	2.91
$t_{f,\text{max}}$ (days)	977.47	526.58	116.93	19.44
$t_{f,\text{avr}}$ (days)	412.67	142.40	23.12	3.75
Dimorphos	0.04%	0.07%	0.22%	0.34%
$t_{f,\text{min}}$ (days)	149.82	78.13	17.85	2.97
$t_{f,\text{max}}$ (days)	883.11	544.72	119.53	17.11
$t_{f,\text{avr}}$ (days)	326.45	194.87	51.02	7.26

where θ_{SD_1} is the phase angle of Didymos with respect to the Sun in the inertial frame and $\theta_{D_j}(j = 1, 2)$ is the phase angle of Didymos's or Dimorphos's self-rotation. The velocity transformation between the reference frames above can be derived by calculating the derivatives of Equation (10).

5. Simulation Results and Analyses

This section presents the results of the ejecta orbital capture simulations. The necessary simulation configurations are outlined first, followed by a detailed demonstration and analysis of the results based on the investigated planar Lyapunov and terminator orbits.

5.1. Simulation Configurations

In this research, the embedded ODE integrator in MATLAB, *ode113*, is utilized for the backward propagation in the ejecta orbital capture simulation, with relative and absolute tolerances set to 2.5×10^{-14} and 1.0×10^{-16}, respectively. The strict tolerances are selected to minimize numerical errors in trajectory propagation, capture sensitive dynamical behavior, and ensure consistent and reproducible results across all trajectory integrations. The four planar Lyapunov families shown in Figure 5 and the four terminator families shown in Figure 6 are selected for analysis. For each planar Lyapunov family, 200 members with their left x-axis intersections evenly distributed are chosen to generate the corresponding stable manifold. Twenty-four sample points evenly distributed along each selected family member are chosen to generate the initial guesses for backward propagation. For the three-dimensional terminator orbits, the same number of evenly distributed sample points is selected along each candidate. These candidate terminator orbits are chosen to ensure that their orbit periods are evenly distributed within the period range of the family. Additionally, a critical phase angle $\theta_{D_1D_2}$, representing the initial phase of Dimorphos in the Didymos-centered inertial frame, is sampled at nine values within the interval $[0°, 360°]$ to investigate the influence of the binary system's geometry on ejecta orbital capture. Thus, for each type of investigated PO, a total of 36 cases are simulated, considering four different strengths of SRP acceleration and nine configurations of the binary system's geometry.

Before proceeding with the analysis of ejection information associated with the two types of candidate orbits, the statistics on ejecta capture rates and the corresponding time of flight t_f are presented separately for the planar Lyapunov and terminator families in Tables 5 and 6. It is observed that the geometry of the binary system has minimal influence on the capture rate for both types of orbits. Thus, the relevant information is not included in the tables. In contrast, the magnitude of SRP acceleration, which corresponds to the size of the spherical particles in both tables, plays a critical role. For both planar Lyapunov and terminator orbits, an increase in SRP acceleration leads to the orbit families being drawn closer to the binary system, thereby resulting in higher capture rates and shorter time of flight. Additionally, captures are more frequently associated with Didymos rather than Dimorphos, which is consistent with their respective dimensions. Furthermore, planar Lyapunov orbits exhibit a considerably higher capture rate compared to the terminator orbits. Such a difference can be attributed to two primary factors. First, the planar Lyapunov family is characterized by complete linear instability, which allows every selected candidate to generate their stable manifold. In contrast, a substantial portion of terminator orbits are linearly stable (as shown in Figure 6) and therefore do not qualify for this analysis based on the invariant manifold. Second, the geometry of the stable manifold associated with planar Lyapunov orbits facilitates easier access to the origin region than that of terminator orbits. Note that the very small $t_{f,\text{min}}$ in Table 5 is associated with the sample points on the candidate planar Lyapunov orbits with a portion located in close proximity to the origin (see Figure 5). Note that for larger ejecta sizes (e.g., 10 cm and 1 m), the associated capture durations and orbit periods as shown in Tables 4, 5, and 6 can approach or exceed the 60 day postimpact analysis window. In such cases, the applicability of the bicircular approximation becomes limited. Nevertheless, the corresponding results are still included to illustrate overall trends and regularities in ejecta behavior across a broader range of SRP sensitivities.

5.2. Results Associated with Planar Lyapunov Orbits

The ejection information associated with planar Lyapunov orbits is presented first. The distribution of ejection velocity, angle, and location for ejecta following the stable manifold of the planar Lyapunov orbits and eventually impacting the surface of Didymos and Dimorphos is shown separately in the two subplots in Figure 8. Additionally, the longitude distribution of these ejecta impacting both asteroid surfaces is further illustrated in the polar coordinates in Figure 9. It is validated that for both asteroids, the strength of SRP acceleration has a minimal influence on the distribution pattern. Thus, the information related to the SRP acceleration is not explicitly presented. Since the recorded ejecta trajectories emanating from the planar Lyapunov orbits are restricted in the xy-plane, the ejection locations are

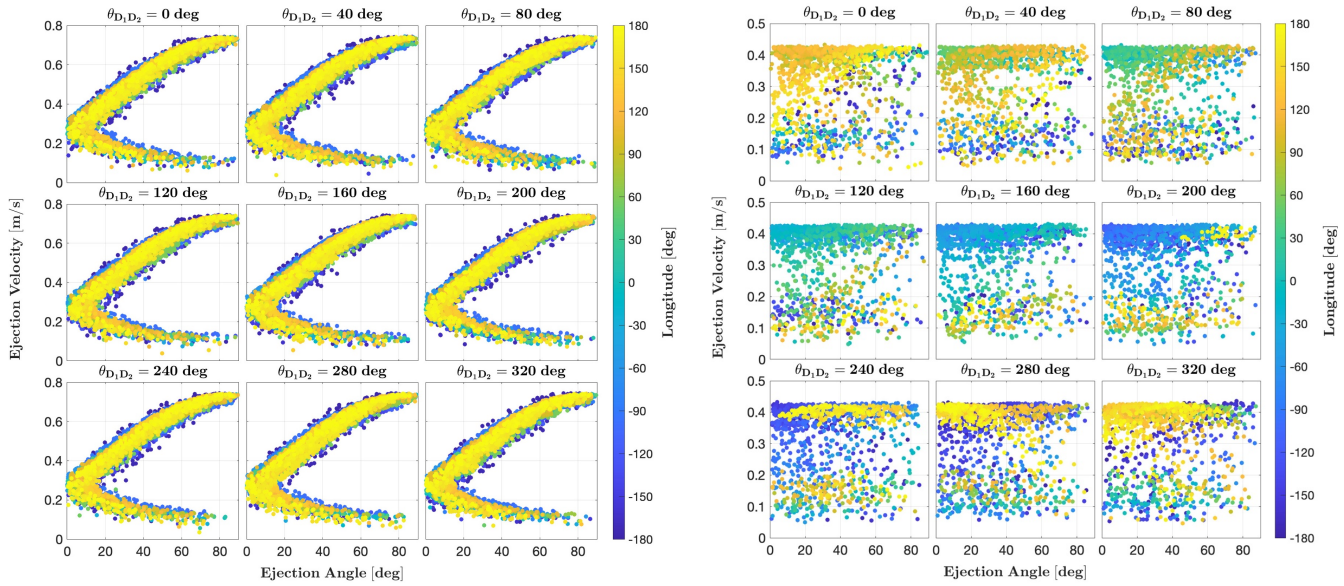

Figure 8. The distribution of ejection velocity, angle, and location for ejecta following the stable manifold of the planar Lyapunov orbits and impacting the surface of (a) Didymos and (b) Dimorphos.

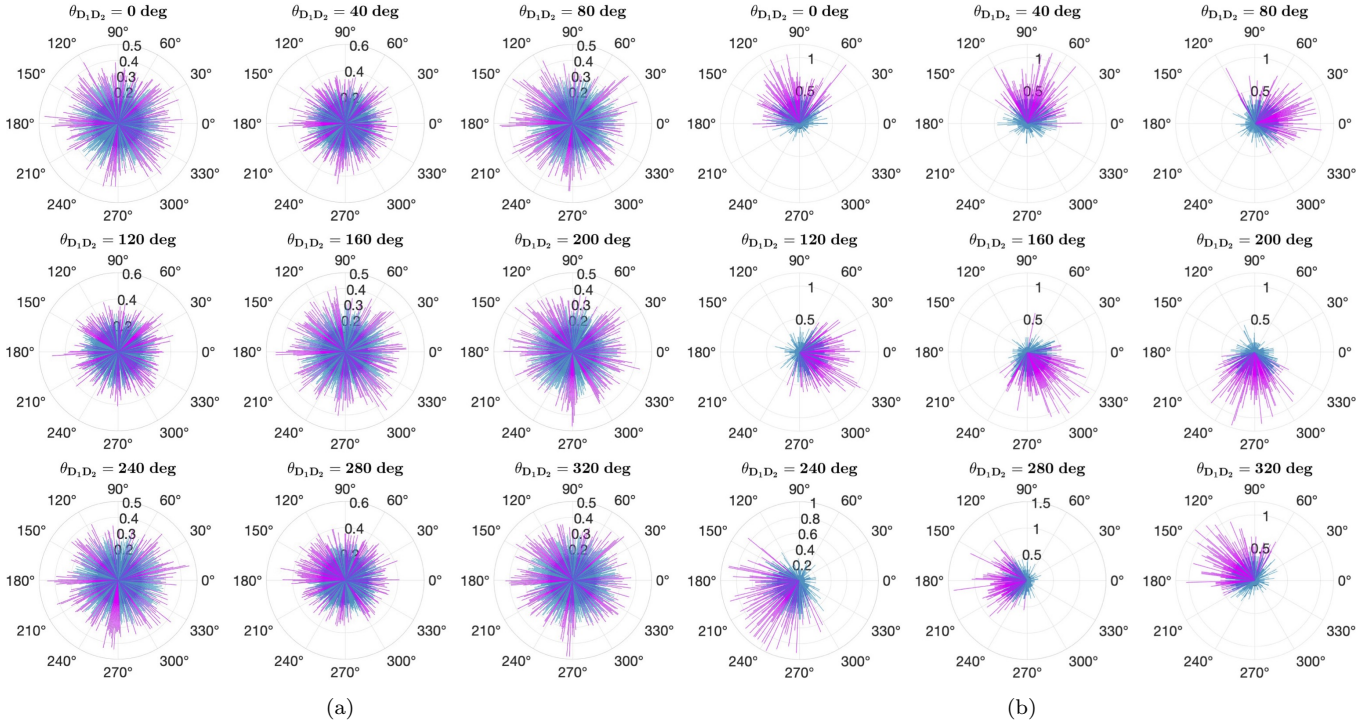

Figure 9. The longitude distribution for ejecta following the stable manifold of the planar Lyapunov orbits and impacting the surface of (a) Didymos and (b) Dimorphos.

concentrated near the equatorial plane of the asteroids, and the longitude is used to represent the ejection location. As shown in Figure 8(a), the distribution of ejection information associated with Didymos exhibits a boomerang-shaped pattern. An intermediate ejection velocity of approximately 0.3 m s^{-1} is observed at an ejection angle of 0°. As the ejection angle increases, the ejection velocity diverges in two directions and reaches its maximum and minimum at the largest ejection angle of 90°. Such a phenomenon can be explained by the geometry of the ejecta trajectory in relation to the ejection cone, which is defined by the local facet normal and ejection velocity vector in the asteroid's body-fixed frame. As depicted in Figure 10(b), when a portion of the ejecta trajectory lies within the ejection cone, part of the ejection velocity is required to counteract the asteroid's self-rotation to achieve a clockwise trajectory. This configuration leads to a higher ejection velocity. Additionally, the maximum ejection velocity is confirmed to be no greater than Didymos's escape speed, as defined within the two-body problem and converted to its body-fixed reference frame, which is approximately

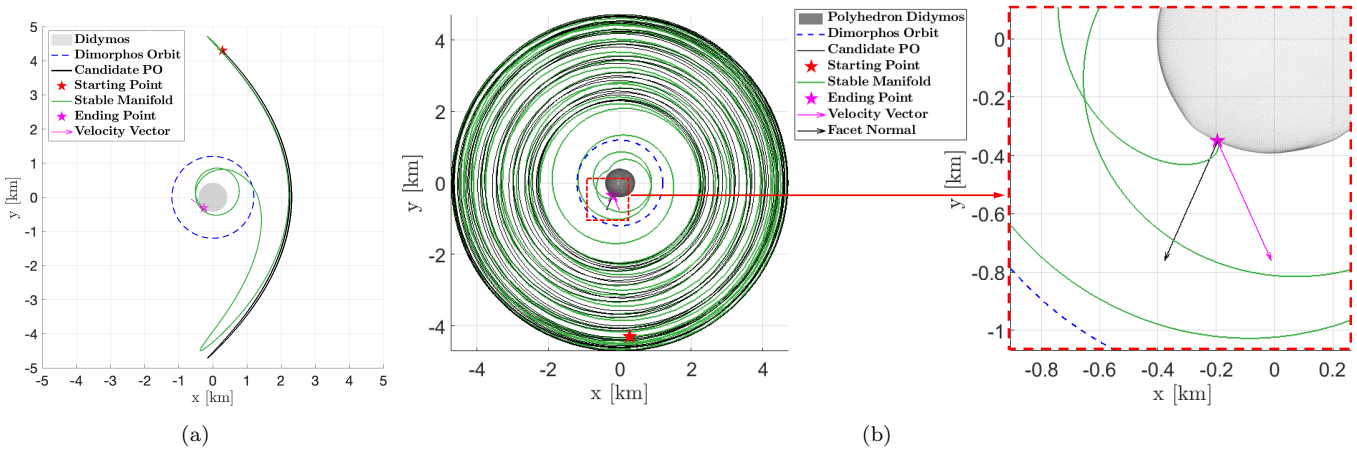

Figure 10. An example of a backward-propagated ejecta trajectory along the stable manifold of a planar Lyapunov orbit eventually impacting Didymos. (a) Trajectory in the Didymos-centered synodic frame. (b) Trajectory in the Didymos-centered body-fixed frame.

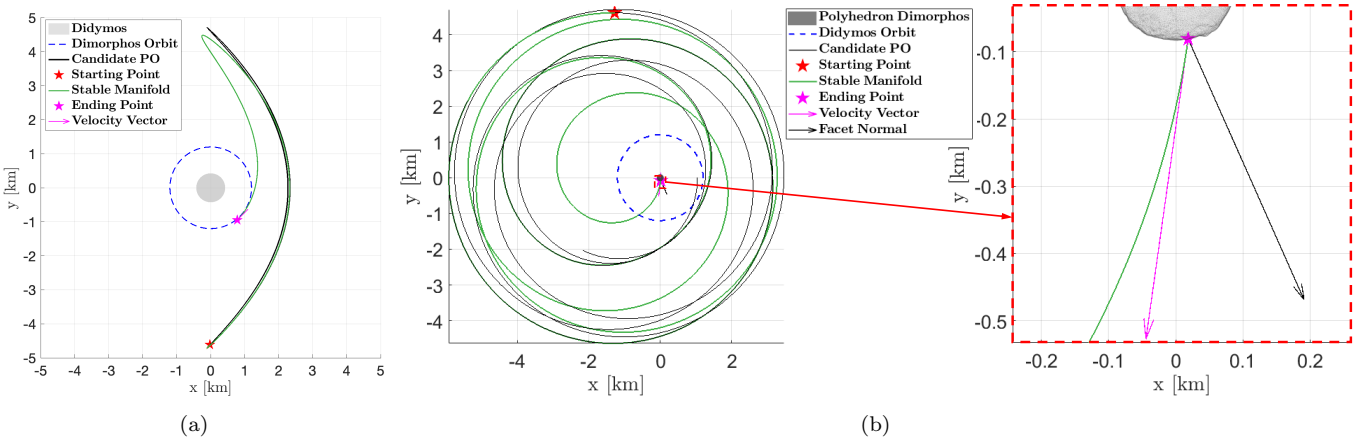

Figure 11. An example of a backward-propagated ejecta trajectory along the stable manifold of a planar Lyapunov orbit eventually impacting Dimorphos. (a) Trajectory in the Didymos-centered synodic frame. (b) Trajectory in the Dimorphos-centered body-fixed frame.

$0.76\,\mathrm{m\,s^{-1}}$. In contrast, when an ejecta trajectory is entirely outside the ejecta cone, which means that the ejection velocity is compensated by the asteroid's rotational speed, it corresponds to a lower ejection velocity (as shown in Figure 11(b)). The explanation above clarifies why there exist two distinct ejection velocities at a nonzero ejection angle. Furthermore, the boomerang-shaped distribution is not limited to the longitude of approximately 150° (as indicated by the yellow dots in Figure 8(a)). This distribution is also observed across other longitude intervals, indicating that the boomerang-shaped pattern applies consistently across all longitudes.

The distribution pattern associated with Dimorphos has a different shape, which can be attributed to Dimorphos being off-center in the synodic frame and its motion being time-dependent. However, it is also verified that the maximum ejection velocity recorded is no larger than Dimorphos's escape speed, as defined within the two-body regime and converted to its body-fixed frame, which is approximately $0.43\,\mathrm{m\,s^{-1}}$. Different from the distribution associated with Didymos, which has minimal dependency upon $\theta_{D_1D_2}$ as shown in Figure 8(a), the distribution of ejection information associated with Dimorphos is explicitly influenced by the geometry of the binary asteroid system. According to Figure 8(b), when $\theta_{D_1D_2}$ varies from 0° to 320°, a color shift in the distribution patterns is clearly observed. The clustered dots in the upper region of each subplot indicate the longitude interval where the majority of ejections occur. To further illustrate the longitudinal distribution pattern, the percentage of ejections within each longitude interval is presented in polar coordinates in Figure 9. The percentages over 0.3% are highlighted in magenta to emphasize areas of higher distribution concentration in the corresponding longitude interval. For the case of Didymos depicted in Figure 9(a), the longitudinal distribution is relatively uniform and not significantly influenced by the binary system's geometry. In contrast, in the case of Dimorphos shown in Figure 9(b), the concentrated longitudinal distribution rotates clockwise from 120° as $\theta_{D_1D_2}$ increases from 0°.

Finally, to complement the aforementioned statistical findings, two examples of backward-propagated ejecta trajectories along the stable manifold of a planar Lyapunov orbit eventually impacting Didymos and Dimorphos are illustrated in Figures 10 and 11, respectively. The two examples are included to demonstrate the validity of the simulation and to provide additional qualitative insight and intuitive understanding of the manifold-based ejecta capture process. The planar Lyapunov orbit is a member of the family depicted in the fourth subplot in Figure 5. The ejecta trajectories are presented in both the Didymos-centered synodic frame and the Didymos/Dimorphos body-fixed frame. As shown in both

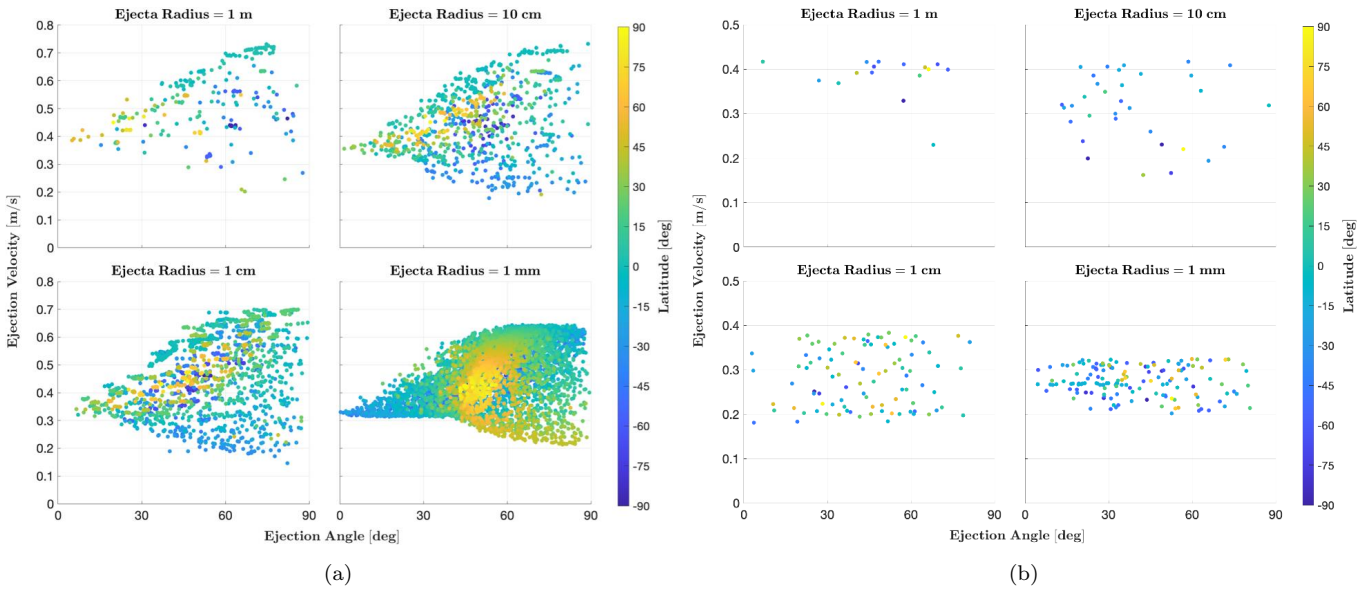

Figure 12. The distribution of ejection velocity, angle, and latitude for ejecta following the stable manifold of the terminator orbits and impacting the surface of (a) Didymos and (b) Dimorphos.

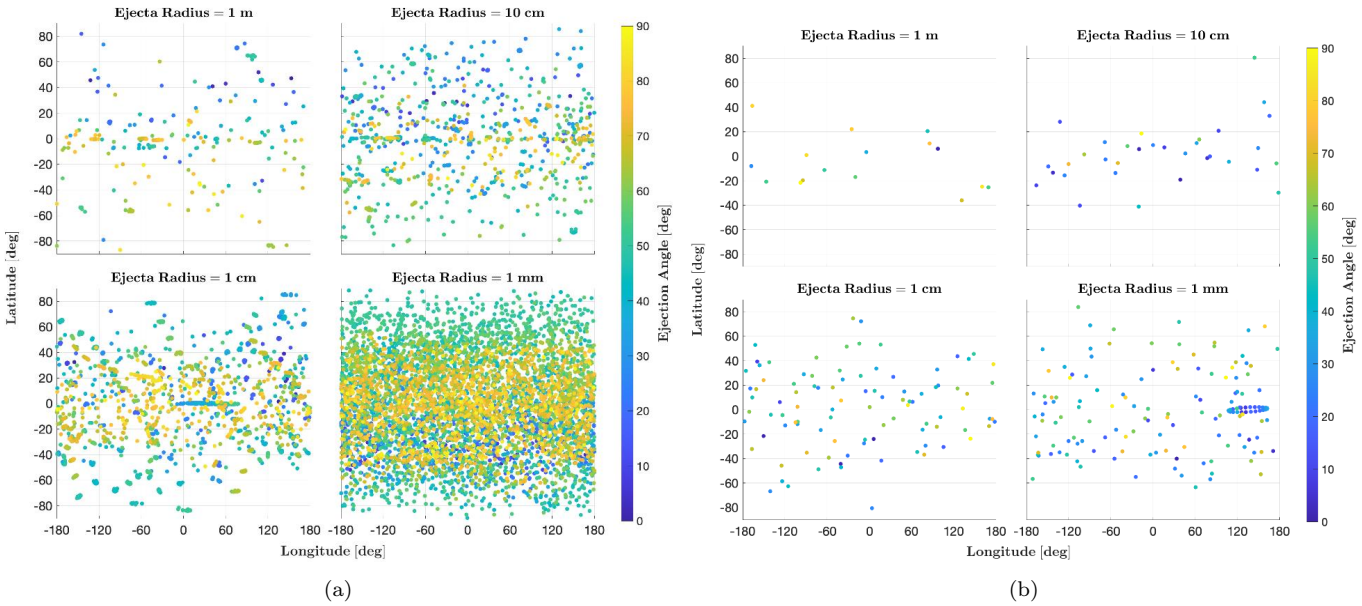

Figure 13. The distribution of ejection location for ejecta following the stable manifold of the terminator orbits and impacting the surface of (a) Didymos and (b) Dimorphos.

figures, the trajectory propagation terminates at the intersection point on the surface of an asteroid. The local facet normal and velocity vector at the intersection are also provided for reference.

5.3. Results Associated with Terminator Orbits

The ejection information associated with terminator orbits is presented in this subsection. The distribution of ejection velocity, angle, and latitude for ejecta following the stable manifold of the terminator orbits and eventually impacting the surface of Didymos and Dimorphos is shown separately in the two subplots in Figure 12. It is observed that for the case of Didymos, the geometry of the binary asteroid system has minimal influence on the distribution pattern in Figure 12(a). In contrast, for Dimorphos, the captured events are too infrequent (as presented in Table 6) to establish any clear relationship with $\theta_{D_1D_2}$. Consequently, the information related to the binary system's geometry is not explicitly presented. As illustrated in Figure 12(a), the distribution of ejection information for Didymos exhibits a cone-shaped pattern. An intermediate ejection velocity of approximately 0.35 m s^{-1} is observed at an ejection angle of 0°. As the ejection angle increases, the ejection velocity diverges in two directions, reaching its maximum and minimum at the largest ejection angle of 90°. On one hand, such a pattern is similar to the one associated with Didymos in Figure 8 and can be partially explained by the geometry of the ejecta trajectory in relation to the ejection cone. On the other hand, the notable differences that exist between the two patterns likely arise from the fact that the terminator orbits are three-dimensional, which

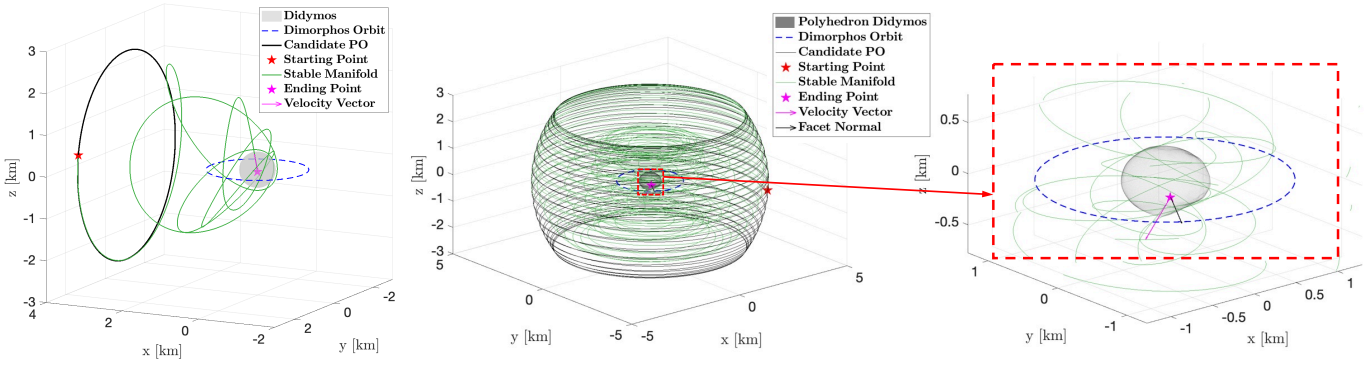

Figure 14. An example of a backward-propagated ejecta trajectory along the stable manifold of a terminator orbit eventually impacting the surface of Didymos. (a) Trajectory in the Didymos-centered synodic frame. (b) Trajectory in the Didymos-centered body-fixed frame.

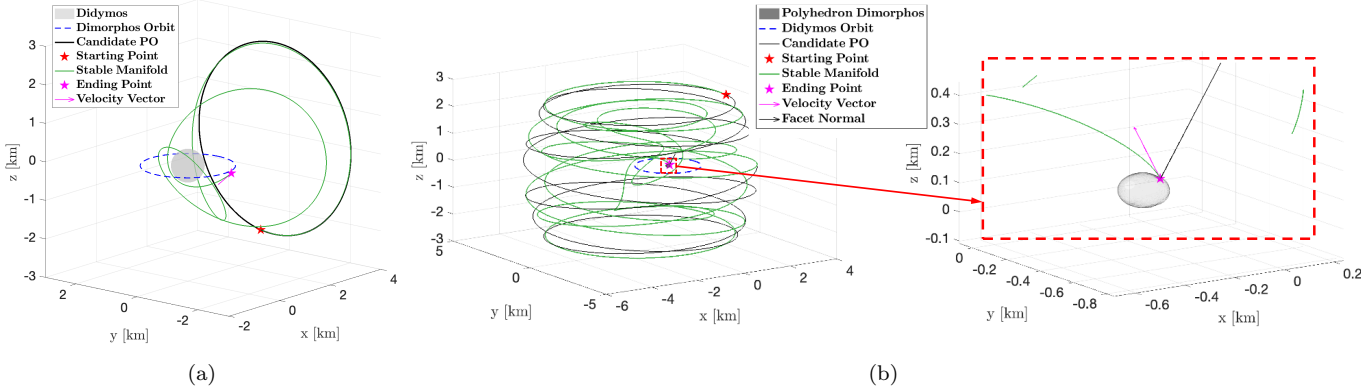

Figure 15. An example of a backward-propagated ejecta trajectory along the stable manifold of a terminator orbit eventually impacting the surface of Dimorphos. (a) Trajectory in the Didymos-centered synodic frame. (b) Trajectory in the Dimorphos-centered body-fixed frame.

introduces more complexity to the structure of the ejection angles. This complexity contributes to the smaller size of the cone shape as the SRP acceleration strengthens. Nonetheless, across all simulated scenarios, the maximum ejection velocity is verified to remain below Didymos's escape speed.

The distribution of ejection location for ejecta following the stable manifold of the terminator orbits and impacting the surface of Didymos and Dimorphos is separately shown in Figures 13(a) and (b). The density of colored dots in both Figure 12 and Figure 13 indicates the frequency of orbital capture observed in the simulations, which is consistent with the results in Table 6. For the simulation scenarios of Didymos where the SRP corresponds to the ejecta particle with a radius of 1 mm, some regularity in the ejection locations can be revealed. By combining the information in the bottom right subplots of Figures 12(a) and 13(a), it can be observed that the ejection events are uniformly distributed along the longitude. Near the polar regions of Didymos, the ejection angle is approximately 45°, while at lower latitudes, the ejection angle either increases or decreases as the latitude approaches 0°.

Finally, to complement the aforementioned statistical findings, two examples of backward-propagated ejecta trajectories along the stable manifold of a terminator orbit eventually impacting Didymos and Dimorphos are illustrated in Figures 14 and 15, respectively. The terminator orbit is a member of the family depicted in the fourth subplot in Figure 6. The ejecta trajectories are presented in both the Didymos-centered synodic frame and the Didymos/Dimorphos body-fixed frame. As shown in both figures, the trajectory propagation terminates at the intersection point on the surface of an asteroid. The local facet normal and velocity vector at the intersection are also provided for reference.

5.4. Implication for Ejecta Generated from DART Impact

The DART spacecraft impacted Dimorphos at a latitude of $8.^{\circ}84 \pm 0.^{\circ}45$S and a longitude of $264.^{\circ}30 \pm 0.^{\circ}47$E, as defined in the Dimorphos body-fixed frame (R. T. Daly et al. 2023). Noticeable ejecta features, including the ejecta cone, cloud, and tails, were observed by the Hubble Space Telescope within 15 days following the DART impact from the binary asteroid system (J.-Y. Li et al. 2023). The observed ejecta cone is consistent with a three-dimensional opening angle of $125^{\circ} \pm 10^{\circ}$ and a centerline at a position angle of $67^{\circ} \pm 8^{\circ}$ (J.-Y. Li et al. 2023). Ejecta features composed of slower dust escaping at less than around $1\,\mathrm{m\,s^{-1}}$ were observed emerging from the base of the ejecta cone (J.-Y. Li et al. 2023). More details about the structure of the ejecta plume are analyzed based on the observation from the LICIACube satellite (E. Dotto et al. 2024). Additionally, recent research indicates that the area affected by the impact and the region from which most of the low-velocity ejecta originates is a substantial portion of Dimorphos's surface (G. Tancredi et al. 2023; S. Raducan et al. 2024). This area is not confined to the close vicinity of the ejecta cone and its surroundings but can encompass nearly a quarter of Dimorphos's impacted hemisphere. Therefore, we will relax the

constraints on the impact location in the subsequent assessment.

Based on the aforementioned observations, the implications of this research for the ejecta generated by the DART impact are assessed. No ejecta trajectories captured by the investigated planar Lyapunov or terminator orbits are detected. By relaxing the constraints on the impact location by 3° in both longitude and latitude, three eligible ejecta trajectories were identified, which are ultimately captured by the planar Lyapunov orbits with the SRP strength corresponding to $r_{\rm ejecta} = 1$ cm. Among the three candidates, the longest transfer time of flight is 39.57 days. The ejecta trajectory will deviate from the associated planar Lyapunov orbit after 1.5 orbital periods, which is approximately 26.5 days. No eligible trajectory is observed to be captured by the terminator orbits in this case. Based on the current study, ejecta particles of the studied sizes that reach a planar Lyapunov or terminator orbit within the investigated time span are unlikely to remain in the vicinity of the orbit and pose a potential hazard to the Hera spacecraft. However, K. Langner et al. (2024) analyzed the evolution of the orbits of a sample of large boulders, similar to those observed by the Hubble Space Telescope (D. Jewitt et al. 2023), and found that about 1% of the simulated objects can remain in highly perturbed orbits within the binary system for at least 4 yr after the ejection. To offer further insights into the ejecta orbital capture resulting from the DART impact, a probability analysis linking the orbital capture results associated with Dimorphos and the DART impact is to be supplemented and conducted in the ephemeris model.

Additionally, note that the thermal radiation pressure is not included in the ejecta dynamics modeled in this work, although it can influence the ejecta's motion in near-surface regions where thermal gradients are pronounced (A. Pedros-Faura 2024). Moreover, the current study does not account for reimpacted or settled dust on the surfaces of Didymos and Dimorphos. With average sizes much smaller than the ejecta investigated in this research, the dust is expected to constitute the most abundant fraction of the ejected material and is particularly sensitive to the SRP (N. N. Gor'kavyi et al. 1997). Preliminary analysis of images from the DRACO camera on board the DART spacecraft has revealed visible structures and patterns that may indicate traces of deposited dust (J. Sunshine et al. 2024). The Hera mission is expected to provide further observational opportunities to investigate the surface accumulation of micrometer-sized grains, which decrease over time as they are dragged farther away. If these dust deposits are successfully identified, orbital dust evolution calculations will become even more significant. Given the weak gravitational environment, the dust is unlikely to simply settle around the crater. Instead, a more complex distribution is likely to form.

6. Conclusions

This research investigates the orbital capture of impact ejecta around the Didymos binary asteroid system. The acceleration and perturbations from various sources are analyzed for the formulation of ejecta dynamics. The ejecta dynamics is subsequently established using an augmented BCRFB model, which incorporates the polyhedron gravity fields of both Didymos and Dimorphos, along with the SRP. The stable manifolds emanating from typical POs in the augmented circular restricted three-body model are utilized to simulate the ejecta orbital capture events.

Comprehensive simulations of ejecta capture for planar Lyapunov and terminator orbits are conducted to investigate the influence of the SRP strength and the binary system's geometry, with key findings summarized as follows. First, the geometry of the binary system has minimal influence on the capture rate for both types of candidate orbits, while an increase in the SRP strength results in a higher capture rate. Second, the orbital capture of ejecta is more frequently associated with Didymos than Dimorphos. Third, the characteristic distribution patterns associated with Didymos and Dimorphos are identified for each type of candidate orbit. The distribution patterns for Didymos are geometry-independent, whereas those for Dimorphos are explicitly governed by the binary system's geometric configuration. Finally, the implications of this research for the ejecta generated from the DART impact are discussed. Based on the current study, ejecta particles of the studied sizes that reach a planar Lyapunov or terminator orbit within the investigated time span are unlikely to remain in the vicinity of the orbit and pose a potential hazard to the Hera spacecraft.

Acknowledgments

This work was supported by a UKRI Future Leaders Fellowship (grant No. MR/W009498/1) awarded to S.S. with the REMORA project (REndezvous Mission for Orbital Reconstruction of Asteroids: A fleet of Self-driven CubeSats for Tracking and Characterizing Asteroids) where X.F. is sponsored. The contribution to this work by E.G.F. was carried out at the Jet Propulsion Laboratory, California Institute of Technology, under a contract with the National Aeronautics and Space Administration (80NM0018D0004). J.M.T.R. acknowledges support from PID2021-128062NB-I00 funded by the Spanish MCIN/AEI.

ORCID iDs

Xiaoyu Fu https://orcid.org/0000-0002-6405-5655
Flavia Saveriano https://orcid.org/0009-0002-6298-5709
Stefania Soldini https://orcid.org/0000-0003-3121-3845
Fabio Ferrari https://orcid.org/0000-0001-7537-4996
Derek C. Richardson https://orcid.org/0000-0002-0054-6850
Masatoshi Hirabayashi https://orcid.org/0000-0002-1821-5689
Alessandro Rossi https://orcid.org/0000-0001-9311-2869
Eugene G. Fahnestock https://orcid.org/0000-0003-1391-5851
Tony L. Farnham https://orcid.org/0000-0002-4767-9861
Arnold Gucsik https://orcid.org/0000-0003-2777-0112
Stravro L. Ivanovski https://orcid.org/0000-0002-8068-7695
Martin Jutzi https://orcid.org/0000-0002-1800-2974
Akos Kereszturi https://orcid.org/0000-0001-6420-510X
Jian-Yang Li https://orcid.org/0000-0003-3841-9977
Francesco Marzari https://orcid.org/0000-0003-0724-9987
Colby C. Merrill https://orcid.org/0000-0002-5566-0618
Fernando Moreno https://orcid.org/0000-0003-0670-356X
Sabina D. Raducan https://orcid.org/0000-0002-7478-0148
Juan Luis Rizos https://orcid.org/0000-0002-9789-1203
Gonzalo Tancredi https://orcid.org/0000-0002-4943-8623
Josep M. Trigo- Rodriguez https://orcid.org/0000-0001-8417-702X

Kleomenis Tsiganis https://orcid.org/0000-0003-3334-6190
Stephan Ulamec https://orcid.org/0000-0002-8856-4622
Yang Yu https://orcid.org/0000-0001-9329-7015
Yun Zhang https://orcid.org/0000-0003-4045-9046
Nancy Chabot https://orcid.org/0000-0001-8628-3176
Andrew Rivkin https://orcid.org/0000-0002-9939-9976
Adriano Campo Bagatin https://orcid.org/0000-0001-9840-2216
Patrick Michel https://orcid.org/0000-0002-0884-1993

References

Broschart, S. B., Lantoine, G., & Grebow, D. J. 2014, CeMDA, 120, 195
Chabot, N. L., Rivkin, A. S., Cheng, A. F., et al. 2024, PSJ, 5, 49
Chappaz, L., Melosh, H. J., Vaquero, M., & Howell, K. C. 2013, AsBio, 13, 963
Cheng, A. F., Agrusa, H. F., Barbee, B. W., et al. 2023, Natur, 616, 457
Daly, R. T., Ernst, C. M., Barnouin, O. S., et al. 2023, Natur, 616, 443
Daly, R. T., Ernst, C. M., Barnouin, O. S., et al. 2024, PSJ, 5, 24
Dotto, E., Deshapriya, J., Gai, I., et al. 2024, Natur, 627, 505
Ferrari, F., Raducan, S. D., Soldini, S., & Jutzi, M. 2022, PSJ, 3, 177
Fu, X., Baresi, N., & Armellin, R. 2022, AdSpR, 70, 96
Fu, X., Soldini, S., Ikeda, H., Scheeres, D. J., & Tsuda, Y. 2024, CeMDA, 136, 29
Gavin, P., Chevrier, V., Ninagawa, K., Gucsik, A., & Hasegawa, S. 2013, JGRE, 118, 65
Gómez, G., Jorba, A., Masdemont, J., & Simó, C. 1993, CeMDA, 56, 541
Gor'kavyi, N. N., Ozernoy, L. M., Mather, J. C., & Taidakova, T. 1997, ApJ, 488, 268
Graykowski, A., Lambert, R. A., Marchis, F., et al. 2023, Natur, 616, 461
Hirsch, M. W., Pugh, C. C., & Shub, M. 1970, BAMaS, 76, 1015
Jet Propulsion Laboratory 2024, JPL Small-body Database Browser: 65803 Didymos (1996 GT), https://ssd.jpl.nasa.gov/tools/sbdb_lookup.html
Jewitt, D., Kim, Y., Li, J., & Mutchler, M. 2023, ApJL, 952, L12
Koon, W. S., Lo, M. W., Marsden, J. E., & Ross, S. D. 2000, Dynamical Systems, the Three-body Problem and Space Mission Design (Berlin: World Scientific)
Langner, K., Marzari, F., Rossi, A., & Zanotti, G. 2024, A&A, 684, A151
Li, J.-Y., Hirabayashi, M., Farnham, T. L., et al. 2023, Natur, 616, 452
Meyer, A. J., Agrusa, H. F., Richardson, D. C., et al. 2023, PSJ, 4, 141
Michel, P., Küppers, M., Bagatin, A. C., et al. 2022, PSJ, 3, 160
Moreno, F., Bagatin, A. C., Tancredi, G., et al. 2023, PSJ, 4, 138
Naidu, S. P., Chesley, S. R., Moskovitz, N., et al. 2024, PSJ, 5, 74
Parker, J. S., & Anderson, R. L. 2014, Low-energy Lunar Trajectory Design, Vol. 12 (Hoboken, NJ: Wiley)
Pedros-Faura, A. 2024, PhD thesis, Univ. Colorado at Boulder
Peña-Asensio, E., Küppers, M., Trigo-Rodríguez, J. M., & Rimola, A. 2024, PSJ, 5, 206
Pravec, P., Scheirich, P., Kušnirák, P., et al. 2006, Icar, 181, 63
Raducan, S., Jutzi, M., Cheng, A., et al. 2024, NatAs, 8, 445
Richardson, D. C., Agrusa, H. F., Barbee, B., et al. 2024, PSJ, 5, 182
Rossi, A., Marzari, F., Brucato, J. R., et al. 2022, PSJ, 3, 118
Scheeres, D. J. 2012, JGCD, 35, 987
Scheeres, D. J. 2016, Orbital Motion in Strongly Perturbed Environments: Applications to Asteroid, Comet and Planetary Satellite Orbiters (Berlin: Springer)
Scheeres, D. J., Durda, D., & Geissler, P. 2002, in Asteroids III, ed. W. F. Bottke, Jr. et al., Vol. 1 (Tucson, AZ: Univ. Arizona Press), 527
Scheeres, D. J., & Marzari, F. 2002, JAnSc, 50, 35
Scheirich, P., & Pravec, P. 2009, Icar, 200, 531
Shampine, L. F., & Gordon, M. K. 1975, Computer Solution of Ordinary Differential Equations: The Initial Value Problem (San Francisco, CA: Freeman)
Soldini, S., Saiki, T., & Tsuda, Y. 2022, FrST, 3, 1017111
Soldini, S., Yamaguchi, T., Tsuda, Y., Takanao, S., & Nakazawa, S. 2020, SSRv, 216, 108
Sunshine, J., Rizos, J., Barnouin, O., et al. 2024, LPICo, 3040, 1332
Tancredi, G., Liu, P.-Y., Campo-Bagatin, A., Moreno, F., & Domínguez, B. 2023, MNRAS, 522, 2403
Thomas, C. A., Naidu, S. P., Scheirich, P., et al. 2023, Natur, 616, 448
Vallado, D. A. 2001, Fundamentals of Astrodynamics and Applications, Vol. 12 (5th ed.; El Segundo, CA: Microcosm Press)
Villegas-Pinto, D., Soldini, S., Tsuda, Y., & Heiligers, J. 2020, Temporary Capture of Asteroid Ejecta into Periodic Orbits: Application to JAXA's Hayabusa2 Impact Event, AIAA Scitech 2020 Forum (Reston, VA: AIAA), 0221
Watanabe, S., Hirabayashi, M., Hirata, N., et al. 2019, Sci, 364, 268
Werner, R. A., & Scheeres, D. J. 1996, CeMDA, 65, 313
Yu, Y., Michel, P., Schwartz, S. R., Naidu, S. P., & Benner, L. A. 2017, Icar, 282, 313